Applied Thermal Engineering 262 (2025) 125220

Contents lists available at ScienceDirect

Applied Thermal Engineering

journal homepage: www.elsevier.com/locate/ate

Research Paper

Thermal-hydrodynamic modeling and design for microchannel cold plates subjected to multiple heat sources

D.J.G. Kuiphuis [a,b,*], M.J. Terpstra [b], W.W. Wits [a,c], W. Rohlfs [a]

[a] University of Twente, Enschede, The Netherlands
[b] Thales Nederland, Hengelo, The Netherlands
[c] Royal NLR - Netherlands Aerospace Centre, Marknesse, The Netherlands

ARTICLE INFO

Dataset link: https://data.mendeley.com/datasets/gwnt75p22n/1

Keywords:
Microchannel cooling
Electronic packages cooling
Thermal management
Electronics cooling

ABSTRACT

With advancing electronics, effective thermal management is crucial to maintain optimal performance and prevent overheating. Addressing the challenge of efficient cooling solutions has become a crucial area of research in modern thermal management. This paper applies and validates the Thermal-Hydrodynamic Model to bridge the knowledge gap on how straight, manifold, and serpentine microchannel configurations meet industry standards. The model predicts critical parameters, including electronic package temperatures, temperature differences across packages, thermal resistances, and pressure drops. Findings underscore the effectiveness of the model in accurately estimating thermal resistances and pressure drops within acceptable error margins compared to numerical simulations. Pressure drop estimates for straight channels consistently remain within a 10% error margin. For serpentine microchannels, the error is within 10% when the Dean number is at maximum 40. Manifold configurations, however, do not meet the 10% criterion. For manifold predictions within a 15% error margin, an Inlet Ratio of at most 0.13, a Velocity Ratio of unity, and low Reynolds numbers are necessary. Furthermore, for thermal resistance estimations, a number of grooves of at least 23 is required to maintain 10% validity. Additionally, a case study demonstrates the model's potential as a practical alternative to simulation-based methods for identifying the optimal cold plate configuration, achieving cooling power requirements at least twice as low as other configurations within the design space.

1. Introduction

With the advancement of electronics across various industries, the importance of thermal management has grown exponentially. Controlling the junction temperature is essential for maintaining the functionality of compact electronic devices. Nowadays, advanced, reliable, and effective cooling technologies are crucial across a diverse range of industries, including mechanical, chemical, aerospace, automotive, energy generation, electronic, and even biological sectors [1–3]. Among the various techniques for managing high-flux electronics effectively, microchannels with liquid cooling emerge as a superior solution that outperforms traditional air cooling technology [4,5] by providing a significantly higher heat transfer coefficient (HTC). This technique emerges as a promising method for achieving efficient and practical cooling solutions, particularly in scenarios in which packages are densely packed [6,7]. Despite its promise, microchannel cooling also poses significant challenges, including fabrication complexities and the necessity for high-grade filtering of the working fluid flowing through the channels [8]. The pioneering work of Tuckerman and Pease [9] in 1981 marked a significant milestone, as they conducted the initial testing of microchannels in a silicon wafer. At a power density of 790 W/cm^2, the substrate temperature rose by 71 °C above the input water temperature, closely matching theoretical predictions.

This study was followed by others centering around the enhancement of the thermal performance of microchannel heat sinks (MCHS). In initial studies, researchers examined how different microchannel configurations, such as triangular, trapezoidal, and circular cross-sections [10–12], impact overall performance. However, the simple channel structure makes it challenging to adapt for high-flux applications. To address this, researchers have proposed alternative channel designs oriented along the stream-wise direction [13–15] and the incorporation of microstructures [16,17]. However, these modifications are associated with substantial increases in pressure drop. For example, Al-Neama et al. [18] conducted a study on serpentine MCHSs. The single-path serpentine configuration improved the average Nusselt number by 35% and reduced thermal resistance by 19% at a flow rate of

* Corresponding author at: University of Twente, Enschede, The Netherlands.
E-mail address: d.j.g.kuiphuis@utwente.nl (D.J.G. Kuiphuis).

https://doi.org/10.1016/j.applthermaleng.2024.125220
Received 27 September 2024; Received in revised form 29 November 2024; Accepted 9 December 2024
Available online 17 December 2024

Nomenclature

A	area (m^2)	$\overline{\alpha}$	average convection HTC (W/m^2K)	seg	segment
C	constant (–)	δ	thickness (m)	sp	spreading
D	diameter (m)	η	dynamic viscosity (Pa s)	str	straight
H	height (m)	κ	empirical parameter (–)	sub	substrate
L	length (m)	λ	thermal conductivity ($W/m\ K$)	th	thermal
L^*	dimensionless thermal length (–)	ρ	density (kg/m^3)	un	undeveloped
				unit	unit cell
L^+	dimensionless hydrodynamic length (–)	*Subscript*		w	wall
		TIM	thermal interface material	3	three-sided
P	pressure (Pa)	avg	average	4	four-sided
$\dot{Q}$	heat transfer rate (W)	cap	capacitance		
R	thermal resistance (K/W)	cell	cold plate unit cell	*Geometric ratio*	
T	temperature (K)	cond	conduction	AR	Aspect Ratio
W	width (m)	conv	convection	CGR	Channel-Groove Ratio
a	equivalent source radius (m)	ch	channel	IR	Inlet Ratio
b	equivalent base radius (m)	cl	coolant line	VR	Velocity Ratio
c_p	specific heat capacity ($J/kg\ K$)	cp	cold plate	WR	Width Ratio
e	error estimate (–)	dev	developed		
f	factor or parameter (–)	f	fluid	*Dimensionless number*	
k	overall HTC (W/m^2K)	fin	fin	Bi	Biot number
m	fin parameter ($1/m$)	gr	groove	De	Dean number
$\dot{m}$	mass flow rate (kg/s)	h	hydraulic	$\overline{Nu}$	average Nusselt number
n	number (–)	in	inlet	Pr	Prandtl number
p	wetted perimeter (m)	man	manifold	Re	Reynolds number
$\dot{q}''$	heat flux (W/m^2)	max	maximum	Re^+	modified Reynolds number
u	velocity (m/s)	min	minimum	f_D	Darcy friction factor
		mod	module		
Φ	dimensionless parameter (–)	ms	microchannel section	*Abbreviation*	
ΔP	pressure drop (Pa)	p	package	THM	Thermal-Hydrodynamic Model
ΔT	temperature difference (K)	serp	serpentine	MPM	MultiPhysics Model
Δx	finite distance (m)	serie	series	HTC	Heat Transfer Coefficient

0.5 l/min compared to straight microchannels. However, this enhancement came with a tenfold increase in pressure drop. To mitigate the pressure drop penalty and improve the temperature uniformity across the area, other researchers focused on designs with shorter microchannel segments. Yang and Zuo [19] designed a novel multi-layer manifold MCHS to manage the surface temperature of Concentrating Photovoltaic cells to obtain higher net output power and prolong lifetime. Their study showed that the surface temperature difference of the cells was below 6.3 °C. Notably, the multi-layer manifold MCHS had a HTC of 8.2 kW/m^2 K and a pressure drop lower than 3 kPa. Shen et al. [20] proposed a novel MCHS design incorporating multi-circuit nested loops to enhance the thermal performance of double-layer microchannel heat sinks (DLMCHS). This design effectively reduced the peak temperature on the substrate, improved temperature uniformity, and has a significant advantage on the overall thermal performance factor, which balances heat transfer and pressure drop. A subsequent study by Shen et al. [21] used impingement jet nested arrays in DLMCHS to improve thermal performance. The findings showed effective thermal control, with a reduction in peak substrate temperature. The proposed design also achieved a higher average Nusselt number compared to traditional impingement jet straight arrays DLMCHS. Despite a higher pressure drop, the overall thermal performance factor still favored the nested channel design. Moreover, Cao et al. [22] introduced a novel design using jet impingement DLMCHS in combination with vertical truncated bifurcations. The study revealed that this design offers substantial improvements over DLMCHS without bifurcations. Specifically, the results demonstrated significantly higher Nusselt numbers and notable enhancements in both pressure drop and thermal uniformity across the substrate. The findings highlight the design's potential to improve cooling efficiency and reliability for electronic chips under high heat flux conditions.

Other studies have focused on integrating microchannels into various components of chipset hardware. Lu et al. [23] proposed embedded manifold microchannels within the chiplet architecture, introducing a cooling approach where microchannels are directly etched onto chips and integrated with 3D-printed manifolds. Under a heat flux of 81 W/cm^2 and a flow rate of 0.8 l/min, the design reduced the average temperature rise to 66.0 °C. The study demonstrated that total thermal resistance decreased with increased flow rates, reaching 0.30 K/W at 0.8 l/min. Additionally, higher flow rates improved temperature uniformity and compensated for height disparity and warpage, ensuring reliability in complex scenarios. Often, in practical applications, multiple heat sources are involved. Bognár et al. [24] focused on tackling the thermal issues associated with heterogeneously integrated packages. Their solution involved a novel cooling approach for 2.5-D heterogeneous packages by integrating microchannels into the silicon interposer. This method, combined with a conventional heat sink and a water flow rate of 100 cm^3/min, reduced CPU temperatures from 109 °C to 44 °C. For four-core CPUs with one core under high load, the temperature dropped by 72.7 °C. The study highlighted the importance of secondary heat flow paths and showed that the proposed system can solve thermal issues in 2.5-D heterogeneous devices. Van Erp et al. [25] developed a novel energy-efficient cooling method for power converters by attaching miniaturized straight microchannel cold plates to transistors. These cold plates were interconnected in parallel to minimize the high-pressure drop associated with microchannels, resulting in a pressure drop of only 2 kPa. The system successfully cooled 20 transistors, achieving a thermal resistance of 0.2 K/W at a flow rate of 1.2 ml/s, effectively managing 300 W of power loss. The results demonstrated a tenfold increase in power density, with potential to reach 30 kW/l. This innovative cooling approach introduces a novel strategy for coengineering cooling and electronics to create more compact and efficient power converters.

In the early stages of microchannel simulation, researchers employed simplified methods to assess heat transfer performance, but some assumptions did not accurately capture real-world conditions. To address this, later studies utilized the classical Navier–Stokes and energy equations to simulate thermal-fluid behavior, which were validated by experimental data [26–28]. Additionally, some researchers investigated flow and heat transfer in microchannels using the Lattice Boltzmann method [29,30], which, despite the high computational cost, did not offer significant advantages over classical simulation approaches. As a result, numerical methods based on the Navier–Stokes and energy equations have proven effective for microchannel applications. Prior research has highlighted that while simulation-based approaches provide valuable insights, their inherently time-consuming nature can impede the design process, thereby underscoring the necessity for a novel tool that expedites the initial design phase.

While existing studies provide valuable insights into microchannel cooling, a significant gap remains in understanding how different configurations align with industry standards, where cold plates are used to manage multiple heat sources. This gap is particularly noticeable when performance is evaluated beyond heat transfer and pressure drop. In high-tech industries, design considerations such as cooling capacity, maximum package temperature, and temperature uniformity across packages are critical. Despite their importance, there is limited knowledge regarding the performance differences between straight, manifold, and serpentine configurations for industry applications, especially when also considering the distribution scheme of the cold plate. To address this gap, there is a need for a tool that streamlines the initial concept design process and offers insightful evaluations of these configurations. This paper discusses the development of an analytical tool that serves as a practical and nearly instantaneous alternative to time-consuming simulation-based methods. Additionally, the paper demonstrates how the model can be used to identify the optimal cooling solution that meets system requirements while minimizing cooling power consumption.

2. Thermal-hydrodynamic model

An analytical Thermal-Hydrodynamic Model (THM) is established to examine how the cold plate geometry affects performance by exploring the geometric features categorized into: macro-scale (distribution scheme), mesoscale (microchannel configurations), and micro-scale (substrate dimensions, channel size, and wall thickness). This is illustrated in Fig. 1. Within a single cold plate module (macro-scale model), there are n_p cold plate unit cells (mesoscale model), each comprising n_{ch} parallel microchannel unit cells (micro-scale model). In this model, the term "package" refers to the electronic component acting as the heterogeneous heat source. The mesoscale microchannel design is attached to the electronic package with a Thermal Interface Material (TIM) positioned between them.

2.1. Model definition

To better understand the impact of design choices regarding cold plate distribution scheme, microchannel configuration, and channel size, the geometrical features are characterized. First, the number of coolant lines n_{cl} is introduced, which characterizes the corresponding distribution scheme associated. The top row of Fig. 1 illustrates the relationship between the number of coolant lines and the corresponding distribution scheme, where $n_{cl} = 1$ represents serial cooling and $n_{cl} = n_p$ parallel cooling. During this study, three different microchannel configurations–manifold, straight, and serpentine–are studied. These configurations are characterized geometrically by the Channel-Groove Ratio (CGR). This ratio quantifies the number of channels accommodated within a single groove (middle row of Fig. 1). A groove in this case refers to the straight machined section where the coolant is flowing through. Serpentine channels utilize multiple grooves within a single channel, while manifolds employ a single groove for a double number of channels. Lastly, a straight configuration utilizes a single groove for each channel. The channel size is characterized by two ratios: the first is the Width Ratio (WR), denoting the ratio between the channel width and wall width, and the second is the Aspect Ratio (AR), representing the ratio between the channel height and width.

2.1.1. Mesoscale

The unit cell of the cold plate, shown in the middle row of Fig. 1, comprises the microchannel section (depicted in gray) and the TIM (depicted in yellow). The package area is equal to the TIM area and given by:

$$A_p = W_p \cdot L_p, \tag{1}$$

where W_p and L_p are the respective width and length of the package.

The cold plate unit cell is assumed to be squared, hence, both the width and length of the microchannel section are equal and given by:

$$L_{ms} = W_{ms} = \sqrt{A_{ms}}, \tag{2}$$

where A_{ms} is the area of the microchannel section.

Finally, the number of parallel microchannels n_{ch} within the cold plate unit cell follows from the number of grooves n_{gr} in relation to the CGR of the design.

2.1.2. Micro-scale

The microchannel unit cell that is situated within the microchannel section of the cold plate is illustrated in the bottom left of Fig. 1. The channel width is derived from the width of the cold plate unit cell and number of grooves, and is computed as follows:

$$W_{ch} = \frac{W_{ms}}{n_{gr}} \cdot \frac{WR}{WR + 1}. \tag{3}$$

Furthermore, both the wall width and channel height are coupled to the channel width by WR and AR, respectively.

For the straight design (configurations where CGR = 1), the channel length is equal to the mesoscale unit cell length:

$$L_{ch,str} = L_{ms}. \tag{4}$$

For the manifold design (configurations where CGR > 1), the influence of the inlets and outlets on the pressure drop is disregarded. The length over which the pressure drop is considered is computed by using the CGR:

$$L_{ch,man} \approx \frac{L_{ms}}{CGR}. \tag{5}$$

This influence is negligible for configurations in which the Inlet Ratio (IR) is small, the Velocity Ratio (VR) between the inlet port and channel section is fixed at unity, and the Reynolds number is small. These parameters result from:

$$IR = \frac{H_{ch}}{L_{ch,man} - 2H_{ch}}, \tag{6}$$

$$VR = \frac{u_{in}}{u_{avg}}, \tag{7}$$

and

$$Re = \frac{\rho_f u_{avg} D_h}{\eta_f}, \tag{8}$$

where H_{ch} denotes the channel height; u_{in} is the average velocity at the manifold inlet; u_{avg} represents the average velocity within the microchannel section; ρ_f depicts the density of the coolant; D_h means the hydraulic diameter; η_f denotes the dynamic viscosity of the fluid.

The hydraulic diameter for rectangular channels is given by:

$$D_h = \frac{4W_{ch} \cdot H_{ch}}{2W_{ch} + 2H_{ch}}, \tag{9}$$

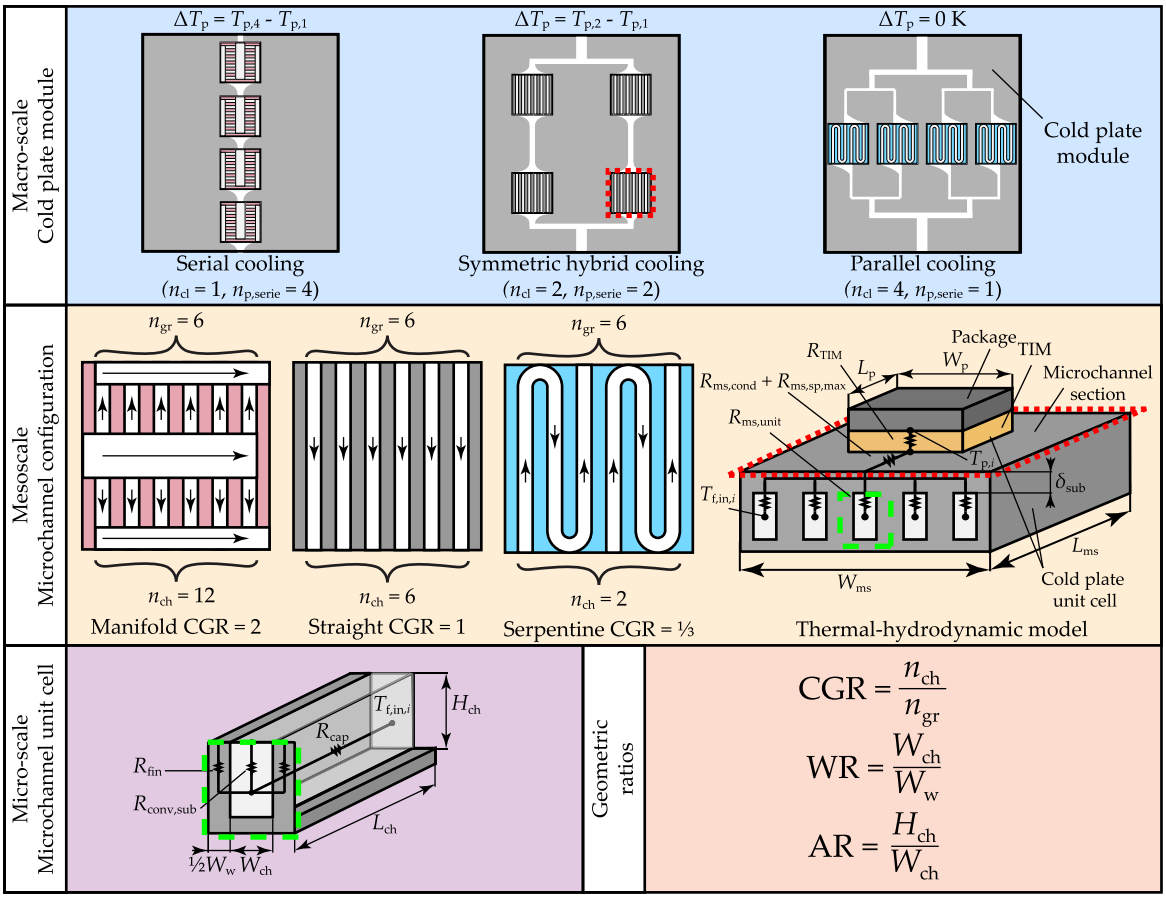

Fig. 1. Key Attributes of the Thermal-Hydrodynamic Model. The top row shows three distribution schemes across a cold plate (macro-scale). The middle rows shows the manifold, straight, and serpentine microchannel configurations and the geometry and thermal resistances within the cold plate unit cell (mesoscale). The bottom row features the microchannel unit cell (micro-scale) and three distinct geometric ratios: Channel-Groove Ratio, Width Ratio, and Aspect Ratio.

and the average velocity, which is coupled to the macro-scale mass flow rate $\dot{m}_{\mathrm{mod}}$, is given by:

$$u_{\mathrm{avg}} = \frac{\dot{m}_{\mathrm{mod}}}{\rho_{\mathrm{f}} \cdot n_{\mathrm{cl}} \cdot n_{\mathrm{ch}} \cdot \left(W_{\mathrm{ch}} \cdot H_{\mathrm{ch}}\right)}. \tag{10}$$

For the serpentine design (configurations where CGR < 1), the effect of the curvature of the bends on the pressure drop is neglected. The bends are approximated as straight sections over which the pressure drop is considered. The total length of the serpentine channel is determined by:

$$L_{\mathrm{ch,serp}} \approx \frac{L_{\mathrm{ms}}}{\mathrm{CGR}} + \left(\frac{1}{\mathrm{CGR}} - 1\right)\left[\frac{\pi}{2}\left(W_{\mathrm{ch}} + W_{\mathrm{w}}\right) - \left(2W_{\mathrm{ch}} + W_{\mathrm{w}}\right)\right]. \tag{11}$$

Neglecting the effect of secondary flow patterns due to the serpentine bends on the calculated pressure drop is justified for configurations with a small Dean number, typically De ≤ 100 for circular pipes [31]. The Dean number for the rectangular serpentine configuration is expressed as:

$$\mathrm{De} = \mathrm{Re}\sqrt{\frac{D_{\mathrm{h}}}{W_{\mathrm{w}} + W_{\mathrm{ch}}}}, \tag{12}$$

where Re is the Reynolds number and the sum of the wall and channel width equals the radius of curvature.

2.1.3. Macro-scale

At the macro-scale, the coolant distribution across the electronics packages is described by the number of parallel coolant lines n_{cl} across the cold plate unit cells. Fig. 1 illustrates the three considered coolant distribution schemes: fully serial, symmetric hybrid, and fully in parallel. The respective number of coolant lines is also given in the figure. The number of electronic packages positioned in series within a single coolant line is determined by:

$$n_{\mathrm{p,serie}} = \frac{n_{\mathrm{p}}}{n_{\mathrm{cl}}}, \tag{13}$$

where n_{p} represents the number of packages.

2.2. Thermal model

A one-dimensional thermal resistance network between the maximum package temperature and the fluid inlet temperature is used to describe the heat transfer rate within a cold plate unit cell. The thermal model is also shown in the middle row of Fig. 1. Heat is assumed to transfer unidirectionally from the package through the TIM before spreading across the microchannel section. The coolant flow through the channels extracts the heat dissipated by the package. The effect of superposition between packages is assumed to be negligible. Assuming a finite number of packages is liquid-cooled according to the distribution of the macroscale model, the maximum temperature at a package i is computed by:

$$T_{\mathrm{p},i} = T_{\mathrm{f,in},i} + \dot{Q}_i \cdot R_{\mathrm{cell}}, \tag{14}$$

where $T_{\mathrm{f,in}}$ depicts the coolant inlet temperature at package i; $\dot{Q}$ denotes the dissipated heat by package i; R_{cell} is the cold plate unit cell thermal resistance.

The cold plate module accommodates a number of packages n_{p}. All accumulated dissipated heat must be transferred away by the coolant. The temperature increase of the coolant across the entire module is

governed by the specific heat capacity $c_{p,f}$ of the coolant and the module mass flow rate $\dot{m}_{mod}$ and calculated according to:

$$\Delta T_{f,mod} = \frac{\sum_{i=1}^{n_p} \dot{Q}_i}{c_{p,f} \cdot \dot{m}_{mod}}. \tag{15}$$

The coolant inlet temperature at the microchannel section is determined by the heat extracted from preceding microchannel sections, mass flow across the microchannel section, and specific heat capacity. This temperature is calculated as:

$$T_{f,in,i} = T_{f,in,mod} + \frac{n_{cl} \cdot \sum_{j=1}^{i-1} \dot{Q}_j}{c_{p,f} \cdot \dot{m}_{mod}}, \tag{16}$$

where $T_{f,in,mod}$ represents the coolant inlet temperature of the module and $\{i \in \mathbb{Z} \mid 1 \leq i \leq n_{p,serie}\}$.

The total thermal resistance between the package temperature and fluid inlet temperature of the cold plate unit cell is computed as:

$$R_{cell} = R_{TIM} + R_{ms,cond} + R_{ms,sp,max} + \frac{1}{n_{ch}} \cdot R_{ms,unit}, \tag{17}$$

where R_{TIM} is thermal resistance of the TIM; $R_{ms,cond}$ represents the conduction resistance; $R_{ms,sp,max}$ means the thermal spreading resistance; $R_{ms,unit}$ depicts the thermal resistance of a single microchannel unit cell.

The impact of temperature-dependent variations in the coolant's thermophysical properties is neglected. This is valid for liquid coolants when the temperature changes along the streamwise direction do not become too large. The average fluid properties used to compute the resistance of the cold plate unit cell are obtained at the mean temperature between the inlet and outlet of the cold plate module:

$$T_{f,prop} = T_{f,in,mod} + \frac{\Delta T_{f,mod}}{2}. \tag{18}$$

For this study, it is assumed that all packages dissipate an equivalent amount of heat. Hence, the maximum temperature difference across packages is determined by:

$$\Delta T_p = T_{p,n_{p,serie}} - T_{p,1}, \tag{19}$$

where $T_{p,n_{p,serie}}$ and $T_{p,1}$ depict the respective temperatures of the last and first-cooled package within a single coolant line.

2.2.1. Thermal resistances

The assumption is made that heat transfer is unidirectional through the TIM before dispersing across the microchannel section. Hence, the thermal resistance of the TIM is calculated by:

$$R_{TIM} = \frac{1}{k_{TIM} A_p}, \tag{20}$$

where k_{TIM} is the TIM's overall HTC.

The conduction resistance is expressed as the ratio of the substrate thickness δ_{sub} to the product of the cold plate's thermal conductivity λ_{cp} and microchannel section area A_{ms} [32]:

$$R_{ms,cond} = \frac{\delta_{sub}}{\lambda_{cp} \cdot A_{ms}}. \tag{21}$$

The bottom row of Fig. 1 shows the one-dimensional thermal resistance network of a single microchannel unit cell. The resistance of a single microchannel unit cell is determined as follows:

$$R_{ms,unit} = \frac{R_{conv,sub} \cdot R_{fin}}{2R_{conv,sub} + R_{fin}} + R_{cap}, \tag{22}$$

where $R_{conv,sub}$ represents the convective resistance from the substrate to the coolant; R_{fin} is the thermal fin resistance from the walls, and in some cases, the bottom of the microchannel section to the fluid; R_{cap} means the capacitance resistance of the coolant flow.

The spreading model by Lee [32] is employed to determine the thermal spreading resistance through the substrate. The total thermal resistance is determined by considering the problem axisymmetric. The model assumes a heat source with uniform heat flux distributed over a small source area A_p, positioned centrally on a larger substrate area A_{ms}. At the bottom of the substrate, a heat sink with a uniform HTC k_{ms} is placed. This assumption holds true if local variations in the thermal resistance of the microchannels are minimal. Heat loss to the surroundings is assumed to be negligible, and the total thermal resistance between the maximum source temperature $T_{sub,max,i}$ and the coolant inlet temperature $T_{f,in,i}$ at the cold plate unit cell is approximated by a simple series resistance network, as shown in Fig. 2.

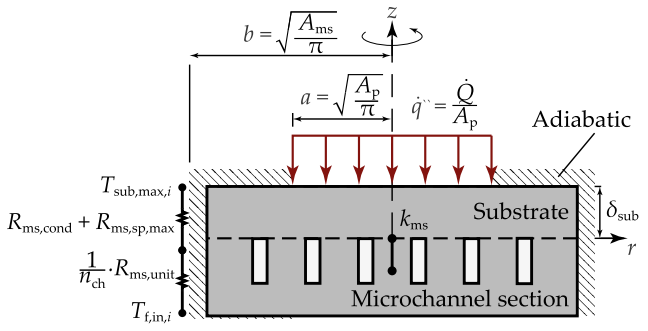

Fig. 2. Thermal spreading model assuming heat spreading through the substrate. A uniform overall heat transfer coefficient is assumed at the interface with the channels. *Source:* Adapted from [32], with modifications for clarity.

By solving Laplace's equation in a two-dimensional cylindrical coordinate system, using four boundary conditions, the temperature distribution can be obtained. For the radial direction, there is symmetry at the center and an adiabatic boundary condition at the outer radius of the base. For the axial direction, the heat flux at the bottom of the substrate is expressed by the overall HTC, and on the top of the substrate a uniform heat flux and an adiabatic boundary condition are employed, depending on the radial position. By using the derived temperature distribution, the total thermal resistance between the maximum source temperature and the coolant inlet temperature is obtained.

The thermal spreading resistance is obtained by subtracting the resistances associated with conduction and the uniform HTC from the obtained total thermal resistance. Hence, the thermal spreading resistance is given by:

$$R_{ms,sp,max} = \frac{1}{\lambda_{cp}\sqrt{\pi A_p}} \left(1 - \frac{a}{b}\right) \Phi, \tag{23}$$

where $a = \sqrt{\frac{A_p}{\pi}}$, and $b = \sqrt{\frac{A_{ms}}{\pi}}$.

The dimensionless parameter Φ yields from [32]:

$$\Phi = \frac{\tanh\left(\frac{\delta_{sub}\kappa}{b}\right) + \frac{\kappa}{Bi}}{1 + \frac{\kappa}{Bi}\tanh\left(\frac{\delta_{sub}\kappa}{b}\right)}, \tag{24}$$

where $\kappa = \pi + \frac{1}{\frac{a}{b}\sqrt{\pi}}$, and $Bi = \frac{k_{ms} b}{\lambda_{cp}}$, and k_{ms} representing the overall HTC between the substrate and the microchannels.

The impact of spreading resistance is most pronounced in the upper section of the substrate. Hence, the overall HTC is calculated from the reciprocal of the product of the microchannel footprint area and the total thermal resistance of the microchannels:

$$k_{ms} = \frac{1}{A_{ms} \cdot \left(\frac{1}{n_{ch}} \cdot R_{ms,unit}\right)}. \tag{25}$$

The convective resistance from the substrate to the fluid, described in Eq. (22), is determined by the inverse of the average convection HTC and the surface area:

$$R_{conv,sub} = \frac{1}{\bar{\alpha} \cdot (W_{ch} \cdot L_{ch})}, \tag{26}$$

with $\bar{\alpha}$ representing the average convection HTC at the channel surface and L_{ch} the length of the respective microchannel.

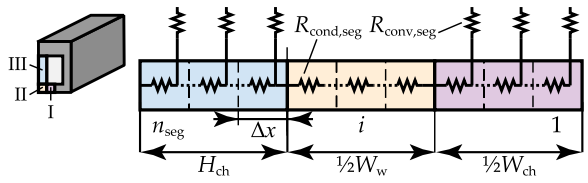

Fig. 3. Discretization of the fin section into n_{seg} segments assuming four-sided heating. Region I illustrates the corner section of the base transporting heat into the fluid by convection, region II the section of the base diffusing heat from region III to I, and region III the walls transporting heat into both the fluid by convection and region II by conduction.

The capacitance resistance is computed as the reciprocal of the product of the fluid's mass flow rate through a microchannel unit cell and the specific heat capacity:

$$R_{cap} = \frac{1}{\rho_f \cdot u_{avg} \cdot (W_{ch} \cdot H_{ch}) \cdot c_{p,f}}. \tag{27}$$

Based on the design and the assumption of heat transfer from three or four sides, thermal fin resistance is calculated analytically or numerically. Three-sided heating is considered when the cover plate is highly insulating or significant thermal contact resistance exists between the base and cover plate. In contrast, four-sided heating applies when the cover plate is highly conductive with negligible thermal contact resistance.

Three-sided heating. In three-sided heating scenarios, the fin resistance is calculated by solving Laplace's equation in a one-dimensional Cartesian coordinate system. This involves a uniform temperature boundary condition at the interface between the fin wall and substrate, alongside assuming an adiabatic tip condition at the interface between the fin wall and cover plate. This gives:

$$R_{fin,3} = \frac{2}{\lambda_{cp}(W_w \cdot L_{ch})\, m \tanh(m H_{ch})}, \tag{28}$$

where the fin parameter m is defined as:

$$m = \sqrt{\frac{2\overline{\alpha}}{\lambda_{cp} W_w}}. \tag{29}$$

Four-sided heating. For four-sided heating scenarios, the contribution of the base is included. The fin section is divided into three domains, as illustrated in Fig. 3. The thermal resistance network is approximated by n_{seg} discrete segments being connected. In this case, the cross-sectional area through which heat diffuses within the walls and the base is assumed to be identical. By assuming a continuous summation of thermal resistances, the following expression is employed to calculate the equivalent thermal resistance of segment i:

$$R_{seg,i} = \begin{cases} R_{cond,seg} + R_{conv,seg} & i = 1 \\ R_{cond,seg} + \frac{R_{conv,seg} \cdot R_{seg,i-1}}{R_{conv,seg} + R_{seg,i-1}} & i \le \frac{W_{ch}+\Delta x}{2\Delta x} \ \vee \ i \ge \frac{W_{ch}+W_w+\Delta x}{2\Delta x} \\ R_{cond,seg} + R_{seg,i-1} & \frac{W_{ch}+\Delta x}{2\Delta x} < i < \frac{W_{ch}+W_w+\Delta x}{2\Delta x} \end{cases}, \tag{30}$$

where Δx is the segment thickness, $R_{cond,seg}$ depicts the segment conduction resistance, $R_{conv,seg}$ means the segment convection resistance, and

$$\{i \in \mathbb{Z} \mid 1 \le i \le n_{seg}\}.$$

As illustrated in Fig. 3, the segment thickness is calculated by summing half the wall width (region I in purple), half the channel width (region II in orange), and the channel height (region III in blue) over the number of segments n_{seg}:

$$\Delta x = \frac{{}^1\!/_2 W_w + {}^1\!/_2 W_{ch} + H_{ch}}{n_{seg}}. \tag{31}$$

The conduction resistance for each segment results from the ratio of the segment thickness and the product of the thermal conductivity and the diffusion area:

$$R_{cond,seg} = \frac{\Delta x}{\lambda_{cp}({}^1\!/_2 W_w \cdot L_{ch})}. \tag{32}$$

The convective thermal resistance is determined by the reciprocal of the average convection HTC and the convective surface area:

$$R_{conv,seg} = \frac{1}{\overline{\alpha}(L_{ch} \cdot \Delta x)}. \tag{33}$$

Finally, the total fin resistance equals the equivalent thermal resistance of the last segment $R_{seg,n_{seg}}$:

$$R_{fin,4} = R_{seg,n_{seg}}, \tag{34}$$

2.2.2. Heat transfer coefficient

The average convection HTC used in Eqs. (26), (29), and (33) is determined from the average Nusselt number:

$$\overline{\alpha} = \frac{\overline{Nu} \cdot \lambda_f}{D_h}, \tag{35}$$

where $\overline{Nu}$ represents the average Nusselt number, and λ_f the coolant thermal conductivity.

The average Nusselt number depends on whether the flow regime is laminar or turbulent. Adding more detail to the thermal model, within the laminar regime both the thermal entrance length and channel's AR influence the coefficient's magnitude.

Laminar flow. When four-sided heating is assumed, the Nusselt number is calculated accordingly:

$$\overline{Nu}_4 = \begin{cases} \overline{Nu}_{un,4}(L^*_{ch}) & L^*_{ch} < L^*_{th} \\ \frac{L^*_{th}}{L^*_{ch}} \cdot \overline{Nu}_{un,4}(L^*_{th}) + \frac{L^*_{ch}-L^*_{th}}{L^*_{ch}} \cdot \overline{Nu}_{dev,4} & L^*_{ch} \ge L^*_{th} \end{cases}, \tag{36}$$

which interpolates the average Nusselt number within the thermally developed regime to avoid discontinuities in the Nusselt correlation. Here $\overline{Nu}_{un,4}$ is the average Nusselt number within the thermally undeveloped regime for four-sided heating; $\overline{Nu}_{dev,4}$ represents the average Nusselt number within the thermally developed regime for four-sided heating; L^*_{ch} depicts the dimensionless thermal channel length; L^*_{th} means the dimensionless thermal entry length.

For three-sided heating, the average Nusselt number is calculated as follows:

$$\overline{Nu}_3 = \frac{\overline{Nu}_{dev,3}}{\overline{Nu}_{dev,4}} \cdot \overline{Nu}_4, \tag{37}$$

which assumes that the ratio of Nusselt numbers for three- and four-sided heating are identical to the ratio when the flow is thermally developed, as demonstrated by Phillips [33]. Here $\overline{Nu}_{dev,3}$ is the average Nusselt number within the developed regime for three-sided heating

The following relationship proposed by Lee and Garimella [34] to calculate the dimensionless thermal entrance length based on the channel's AR is used:

$$\begin{aligned} L^*_{th} = &-1.275 \cdot 10^{-6} AR^6 + 4.709 \cdot 10^{-5} AR^5 \\ &- 6.902 \cdot 10^{-4} AR^4 + 5.014 \cdot 10^{-3} AR^3 \\ &- 1.769 \cdot 10^{-2} AR^2 + 1.845 \cdot 10^{-2} AR \\ &+ 5.691 \cdot 10^{-2}. \end{aligned} \tag{38}$$

The dimensionless thermal channel length is introduced as the ratio of the channel length to the product of the Reynolds number, Prandtl number, and hydraulic diameter [34]:

$$L^*_{ch} = \frac{L_{ch}}{Re\ Pr\ D_h}, \tag{39}$$

where the Prandtl number Pr is determined by:

$$\mathrm{Pr} = \frac{\eta_f \cdot c_{p,f}}{\lambda_f}. \tag{40}$$

The following correlation for the average Nusselt number for thermally undeveloped flow in the case of four-sided heating is provided [34]:

$$\overline{\mathrm{Nu}}_{un,4}\left(L^*\right) = \frac{1}{C_1 \cdot (L^*)^{C_2} + C_3} + C_4, \tag{41}$$

which is valid for $1 \leq \mathrm{AR} \leq 10$. The constants C_1 to C_4 are given as: $C_1 = -2.757 \cdot 10^{-3}\mathrm{AR}^3 + 3.274 \cdot 10^{-2}\mathrm{AR}^2 - 7.464 \cdot 10^{-5}\mathrm{AR}^1 + 4.476$, $C_2 = 6.391 \cdot 10^{-1}$, $C_3 = 1.604 \cdot 10^{-4}\mathrm{AR}^2 - 2.622 \cdot 10^{-3}\mathrm{AR}^1 + 2.568 \cdot 10^{-2}$, and $C_4 = 7.301 - \frac{1.311 \cdot 10^1}{\mathrm{AR}^1} + \frac{1.519 \cdot 10^1}{\mathrm{AR}^2} - \frac{6.094}{\mathrm{AR}^3}$.

When the flow is thermally developed, the following Nusselt correlation is provided for the case of four-sided heating [34]:

$$\overline{\mathrm{Nu}}_{dev,4} = 8.235\left(1 - \frac{2.0421}{\mathrm{AR}} + \frac{3.0853^2}{\mathrm{AR}} - \frac{2.4765^3}{\mathrm{AR}} + \frac{1.0578^4}{\mathrm{AR}} - \frac{0.1861^5}{\mathrm{AR}}\right), \tag{42}$$

and for the case of three-sided heating [35]:

$$\overline{\mathrm{Nu}}_{dev,3} = 8.235\left(1 - \frac{1.883}{\mathrm{AR}} + \frac{3.767^2}{\mathrm{AR}} - \frac{5.814^3}{\mathrm{AR}} + \frac{5.361^4}{\mathrm{AR}} - \frac{2.0^5}{\mathrm{AR}}\right). \tag{43}$$

Turbulent flow. In the turbulent regime, the influences stemming from the channel's shape, thermal entrance length, and whether subjected to three- or four-sided heating are less pronounced on the average convection HTC. Therefore, the average Nusselt number is determined using the Gnielinksi correlation [36]:

$$\overline{\mathrm{Nu}} = \frac{\left(\frac{f}{8}\right)(\mathrm{Re} - 1000)\,\mathrm{Pr}}{1 + 12.7\sqrt{\frac{f}{8}}\left(\mathrm{Pr}^{2/3} - 1\right)}\left[1 + \left(\frac{D_h}{L_{ch}}\right)^{2/3}\right], \tag{44}$$

where factor f is calculated from [36]:

$$f = \left[1.82\log(\mathrm{Re}) - 1.64\right]^{-2}. \tag{45}$$

Transitional flow. Both laminar and turbulent correlations are applicable for estimating the Nusselt number at Re equal to 2300. Yet, at this Reynolds number, the turbulent value is roughly two times larger than the laminar Nusselt number. This disparity results in a discontinuity in the Nusselt number function. In this study, it is assumed that the regime is fully turbulent for $\mathrm{Re} \geq 3500$. For the transition regime with $2300 \mathrm{Re} < 3500$, the average Nusselt number is linearly interpolated:

$$\overline{\mathrm{Nu}} = \frac{\mathrm{Re} - 2300}{1200} \cdot \left(\overline{\mathrm{Nu}}_{tur} - \overline{\mathrm{Nu}}_{lam}\right) + \overline{\mathrm{Nu}}_{lam}, \tag{46}$$

where $\overline{\mathrm{Nu}}_{lam}$ is the average Nusselt number applicable for laminar flow, and $\overline{\mathrm{Nu}}_{tur}$ depicts the average Nusselt number for turbulent flow.

2.3. Hydrodynamic model

The total pressure drop across the cold plate module is calculated according to:

$$\Delta P_{mod} = n_{p,serie} \cdot \Delta P_{cell}, \tag{47}$$

where the pressure drop across the cold plate unit cell ΔP_{cell} is determined by:

$$\Delta P_{cell} = \frac{f_D \rho_f u_{avg}^2}{2 D_h} L_{ch}, \tag{48}$$

where f_D is the Darcy friction factor.

2.3.1. Friction factor

The Darcy friction factor is contingent on whether the flow is assumed to be hydrodynamically developed at the inlet. If not, the pressure drop is also affected by effects arising from the undeveloped region, which is accounted for by the apparent Darcy friction factor $f_{D,app}$.

Table 1
Curve-fit constants for Eq. (50) based on friction factor data in the entrance region of rectangular ducts provided by Phillips [38]. Table taken from [37].

AR	Constants					
	C_5	C_6	C_7	C_8	C_9	C_{10}
1.0	141.97	−7.0603	2603	1431.7	14 364	−220.77
2.0	142.05	−5.4166	1481	1067.8	13 177	−108.52
5.0	142.1	−7.3374	376.69	800.92	14 010	−33.894
≥ 10.0	286.65	25.701	337.81	1091.5	26 415	8.4098

Laminar flow. Shah and London [35] provided the following relationship for the fully developed laminar friction factor based on the AR of rectangular ducts:

$$f_D = \frac{96}{\mathrm{Re}} \cdot \left(1 - \frac{1.3553}{\mathrm{AR}} + \frac{1.9467}{\mathrm{AR}^2} - \frac{1.7012}{\mathrm{AR}^3} + \frac{0.9564}{\mathrm{AR}^4} - \frac{0.2537}{\mathrm{AR}^5}\right). \tag{49}$$

Kandlikar et al. [37] recommended the use of Eq. (50) to estimate the apparent friction factor across different ARs as a function of the dimensionless hydrodynamic length. This function is developed from friction factor data in the entrance region of rectangular ducts provided by Phillips [38].

$$f_{D,app} = \frac{1}{\mathrm{Re}} \frac{C_5 + C_7\left(L_{ch}^+\right)^{1/2} + C_9 L_{ch}^+}{1 + C_6\left(L_{ch}^+\right)^{1/2} + C_8 L_{ch}^+ + C_{10}\left(L_{ch}^+\right)^{3/2}}, \tag{50}$$

where L_{ch}^+ is the dimensionless hydrodynamic length. Constants C_5 to C_{10} in Eq. (50) depend on the AR and are listed in Table 1. In cases where the channel AR is not covered by the curve fit, linear interpolation is utilized.

The dimensionless hydrodynamic length is determined by [37]:

$$L_{ch}^+ = \frac{L_{ch}}{\mathrm{Re}\, D_h}. \tag{51}$$

Turbulent flow. Phillips [38] presented an equation for the Darcy friction factor to cover both the undeveloped and developed flow regions:

$$f_{D,app} = C_{11}\left(\mathrm{Re}^+\right)^{C_{12}}, \tag{52}$$

where $C_{11} = 0.3716 + \frac{4.06448 \cdot D_h}{L_{ch}}$, and

$C_{12} = -0.26800 - \frac{0.32930 \cdot D_h}{L_{ch}}$. For rectangular channel geometries in the turbulent regime, Jones Jr. [39] suggested the following modified Reynolds number:

$$\mathrm{Re}^+ = \left(\frac{2}{3} + \frac{11}{24 \cdot \mathrm{AR}} \cdot \frac{2 \cdot \mathrm{AR} - 1}{\mathrm{AR}}\right) \cdot \mathrm{Re}. \tag{53}$$

Transitional flow. Similar to the thermal model, within the transitional flow regime, the Darcy friction is linearly interpolated using laminar and turbulent values:

$$f_D = \frac{\mathrm{Re} - 2300}{1200} \cdot \left(f_{D,tur} - f_{D,lam}\right) + f_{D,lam}, \tag{54}$$

where $f_{D,lam}$ is the Darcy friction factor applicable for laminar flow, and $f_{D,tur}$ depicts the Darcy friction factor for turbulent flow.

2.4. Validation and verification

The THM performance is verified and validated by assessing both the estimated thermal resistance and pressure drop of the microchannel sections. These two parameters form the foundation for the model's other predictions, including the temperature of the electronic packages, the temperature difference across the packages, and the pressure drops across the cold plate modules. Besides, the relative error estimate for an entire cold plate module matches that of a single cold plate unit cell. This occurs because the relative errors accumulate in a linear manner throughout the series, leading to an overall relative error that remains consistent. In the validation and verification study, an error margin of 10% compared to numerical simulations was preferred for practical

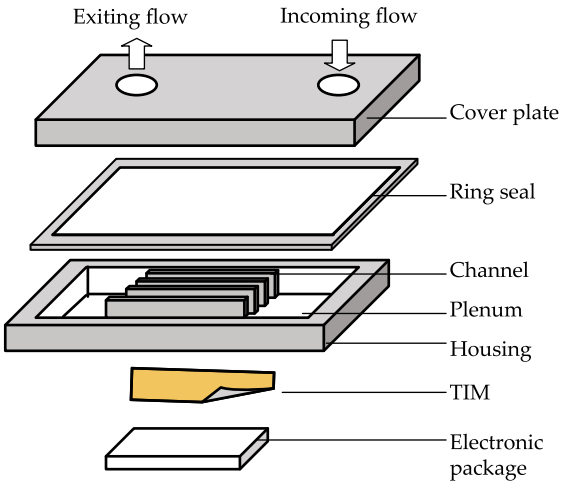

Fig. 4. Overview of the experimental setup from Zhang et al. [40]. Adapted with modifications for clarity.

use during the initial design process. However, in cases where this threshold could not be consistently met, an error margin of up to 15% was considered acceptable.

The thermal resistance and pressure drop for multiple cases are calculated and compared with bespoke numerical MultiPhysics Model (MPM) simulations using COMSOL Multiphysics® 5.6. Moreover, to validate both the THM and numerical simulations, the experiment conducted by Zhang et al. [40] was modeled and results were compared.

The discrepancies between studies are quantified using the following relative error function:

$$e = \left(\frac{f_2 - f_1}{f_1} \right) \cdot 100\%, \tag{55}$$

where f_1 and f_2 are the values of parameters for two datasets.

2.4.1. Experimental database

The experimental study by Zhang et al. [40] involved an aluminum heat sink with 21 straight channels. The experimental setup is shown in Fig. 4. The electronic package dissipated 60 W of heat. To make the experiment compatible with both models, some assumptions are made. The heat sink conductivity is assumed at 238 W/m K since copper was used. Besides, water properties are taken at 20 °C. Moreover, hydrodynamically undeveloped flow at the inlet is assumed, given that the coolant constricts when flowing from a reservoir into the channels. Also, three-sided heating is assumed, because an acrylic cover plate is fastened by four screws and sealed with a Viton O-ring.

2.4.2. Numerical verification

Multiple models were generated using a brute-force search algorithm to identify the optimal WR, AR, number of coolant lines n_{cl}, substrate thickness δ_{sub}, number of grooves n_{gr}, and footprint area A_{ms}. The algorithm aimed at minimizing the package temperature of the last-cooled package $T_{p,n_{p,serie}}$ while adhering to the module mass flow rate requirement, the module pressure drop requirement, and size constraints. The CGR of both manifold and serpentine configurations were iteratively adjusted until the optimal coolant distribution is fully serial ($n_{cl} = 1$) or fully parallel ($n_{cl} = n_p$).

The straight and serpentine configuration models are tailored for two distinct manufacturing methods: micro-milling of aluminum, with a minimum channel width of 0.2 mm, a minimum wall width of 0.3 mm, and a maximum AR of 3, and CNC machining aluminum, with a minimum channel width of 2 mm, a minimum wall width of 1.6 mm and a maximum AR of 4. A negligible thermal contact resistance with the cover plate is assumed for both methods, hence employing the four-sided heating method.

Table 2
Model validation study.

Parameter		Experiment [40]	THM	Numerical
R_{cell}	(K/W)	0.399	0.427 (7.1%)	0.403 (1.6%)
ΔP_{cell}	(kPa)	6.2	6.1 (2.4%)	6.0 (3.3%)

Notably, within the given design space, no manifold configurations were identified for CNC machining that could meet the pressure drop requirement. Consequently, a third fabrication method is included to evaluate different manifold configurations: micro-milling of copper. This method adheres to the same manufacturing constraints as micro-milling of aluminum and operates under the assumption of high thermal contact resistance with the cover plate, therefore employing the three-sided heating approach.

Model definition. The numerical model of the straight micro-milled aluminum configuration is illustrated in Fig. 5. Similar models are utilized for the other configurations. Manifold configurations are modeled with inlet and outlet ports at the bottom, and their port dimensions are adjusted to achieve a VR of unity, see Eq. (7). The thermal conductivity of the TIM element is modeled to match the one-dimensional thermal characteristics of Eq. (20).

Governing equations. A three-dimensional conjugate heat transfer model is employed to simulate both heat transfer and fluid flow phenomena. The analysis is conducted under steady-state conditions, assuming incompressible laminar flow throughout the model. Turbulence models are not utilized because all optimal configurations operate within the laminar flow regime. However, turbulence models are included in the framework for potential application in cases involving higher mass flows for example. Additionally, thermal radiation and viscous dissipation are disregarded, and a continuum assumption is applied. The heat transfer within the fluid domain is governed by the following equation:

$$\rho_f c_{p,f} \vec{u}_f \cdot \nabla T_f = \lambda_f \nabla^2 T_f, \tag{56}$$

where $\vec{u}_f$ represents the coolant velocity vector, and T_f means the temperature in the fluid domain.

The equation describing steady-state heat conduction in the solid domains is as follows:

$$\lambda_s \nabla^2 T_s = 0. \tag{57}$$

where T_s is the temperature in the solid domain. The continuity equation and the Navier–Stokes equations for incompressible fluids are used to solve the governing equations for the fluid domain.

The material and thermophysical properties are considered to be temperature-independent and are taken at the average temperature between the microchannel section inlet and outlet.

Boundary conditions. The TIM experiences a uniform and constant heat flux from the top. Symmetry conditions are employed wherever feasible to minimize the computational time for manifold and straight configurations. The temperature and heat flux of the fluid at the fluid–solid interface equals those of the solid. The fluid temperature at the inlet is set to the inlet temperature of the last-cooled package, and the outflow boundary condition is set at the channel outlet. The remaining outer boundaries are thermally isolated. The fluid velocity is uniformly distributed at the inlet of the channels, while the outlet pressure is maintained at zero. Along the channel walls, a non-slip boundary condition is set.

3. Model validity

The findings from the THM and numerical simulation demonstrate satisfactory agreement with the experimental outcomes, as highlighted

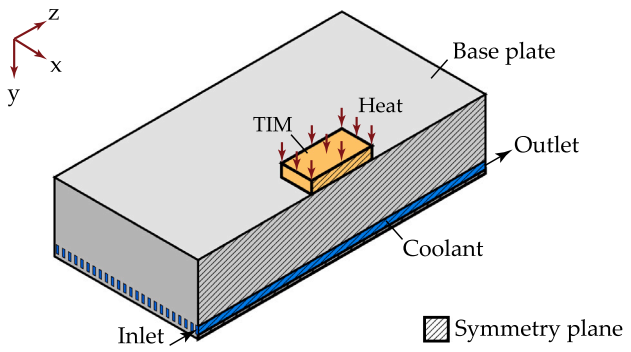

Fig. 5. Coolant, cold plate, and TIM subdomains of the numerical model straight micro-milled aluminum configuration.

Table 3
Comparison of thermal resistance of a cold plate unit cell (R_{cell}) and pressure drop across the microchannel section (ΔP_{cell}) obtained by Thermal-Hydrodynamic Model and numerical simulations for various manifold, straight, and serpentine configurations.

Configuration		Optimal model characteristics				Numerical		THM	
		n_{gr} (–)	Re (–)	IR (–)	De (–)	R_{cell} (K/W)	ΔP_{cell} (kPa)	R_{cell} (K/W)	ΔP_{cell} (kPa)
Micro-milled aluminum	CGR = 4	23	149	0.60	–	10.99	4.6	1.04 (5.1%)	3.1 (32.7%)
Micro-milled copper	”	88	31	0.06	–	0.70	7.1	0.71 (2.3%)	6.3 (12.2%)
Micro-milled aluminum	CGR = 1/7	63	40	–	29	1.46	203.3	1.30 (9.7%)	200.0 (1.6%)
CNC machined aluminum	”	7	1185	–	1071	1.01	13.7	1.19 (17.5%)	6.3 (54.4%)
Micro-milled aluminum	CGR = 1	47	59	–	–	1.05	26.3	1.12 (6.9%)	25.0 (4.8%)
CNC machined aluminum	”	1	2242	–	–	1.18	2.9	1.50 (27.7%)	3.1 (9.2%)

in Table 2. The THM estimates a 7.1% higher thermal resistance compared to the experimental results, and the predicted pressure drop deviates by 2.4%. The numerical simulation estimates a 1.6% higher thermal resistance compared to the experimental results, and the predicted pressure drop deviates by 3.3%.

Table 3 highlights three cases with two designs sharing an identical CGR (4, 1/7, and 1). Note that for each case, the THM is used to find an optimal configuration after which this configuration was modeled numerically. The key parameters of these models are listed in Table 3. For the micro-milled copper manifold, micro-milled aluminum straight, and micro-milled aluminum serpentine configurations, the THM provides comparable thermal resistance and pressure drop results to the numerical simulations, while for micro-milled aluminum manifold, CNC machined aluminum straight, and CNC machined aluminum serpentine configurations, the THM results significantly surpassed the considered 10% validity range.

The results show a pronounced impact of manifold in- and outlet ports on the THM estimates. The impact of the inlet and outlet ports can be correlated to the IR of the design, as defined in Eq. (6). A large IR implies that the inlets and outlets occupy and influence a substantial portion of the straight microchannel section length. Additionally, the error estimate of the THM is affected by the serpentine bends, whose impact can be associated with the magnitude of the Dean number, as given in Eq. (12). A high Dean number indicates significant secondary flow effects, which enhance mixing and disrupt the boundary layer, affecting pressure drop and heat transfer characteristics. Lastly, the number of grooves also impacts the error estimate of the THM, as their magnitude influences the validity of the assumption of a uniform HTC made for heat spreading across the microchannels. As shown in Fig. 6, an increase in the IR and Dean number, and a decrease in the number of grooves amplify the relative discrepancies between the THM and numerical simulations. The impact of these characteristics is further discussed in the next sections.

3.1. Impact of manifold in- and outlets on pressure drop

Two manifold CGR = 4 configurations with both a low Reynolds number are highlighted in Table 3. For the configuration with IR = 0.60 (micro-milling of aluminum), the THM exhibits an underestimation of the pressure drop by 32.7%. Conversely, for the same CGR with IR = 0.06 (micro-milling of copper), the pressure drop underestimation reduces to 12.2%. This is due to the impact of the IR at low Reynolds numbers, in which both IRs result from the fixation of VR = 1.

The resulting pressure distribution diagrams of the two manifold configurations are presented in Fig. 7. The figure illustrates the impact of the IR on the pressure drop. For the case with IR = 0.60, the pressure drop is primarily concentrated at the in- and outlet ports due to the fluid turning 90°. The THM however neglects this effect and only accounts for a pressure drop due to flow in the straight sections. Conversely, for the case where IR = 0.06, a more gradual pressure drop is observed along the channel, indicating the more predominant influence of the straight section on pressure drop. Hence, manifold configurations characterized by a higher IR exhibit a higher error estimate in pressure drop at small Reynolds numbers.

The verification study revealed that the THM's pressure drop estimations showed relative discrepancies exceeding 10% for all manifold configurations. As a result, an error margin of up to 15% was considered for estimating the pressure drop of manifold configurations. The configuration with an IR of 0.13 (shown in Fig. 6) is the configuration with the largest IR for which the relative discrepancy remains below 15.0%, with the underestimation in pressure drop being 14.0%. Thus, the validity of the correlations employed by the THM in estimating the pressure drop across manifold microchannels remains within a 15% margin of error when IR $\leq$ 0.13 and VR = 1 at small Reynolds numbers.

3.2. Impact of serpentine bends on pressure drop

The THM shows the largest relative difference in pressure drop error estimate for the serpentine CGR = 1/7 configurations, with an underestimation of 54.4% when De = 1071 (CNC aluminum) and 1.6% when De = 29 (micro-milling of aluminum), as highlighted in Table 3.

The pressure drop resulting from the serpentine bends is neglected by the THM. Fig. 8 depicts pressure distributions for these configurations, revealing that the largest pressure drops are observed in the bent regions for the case with De = 1071. This is attributed to the increased friction caused by the centrifugal force acting on the

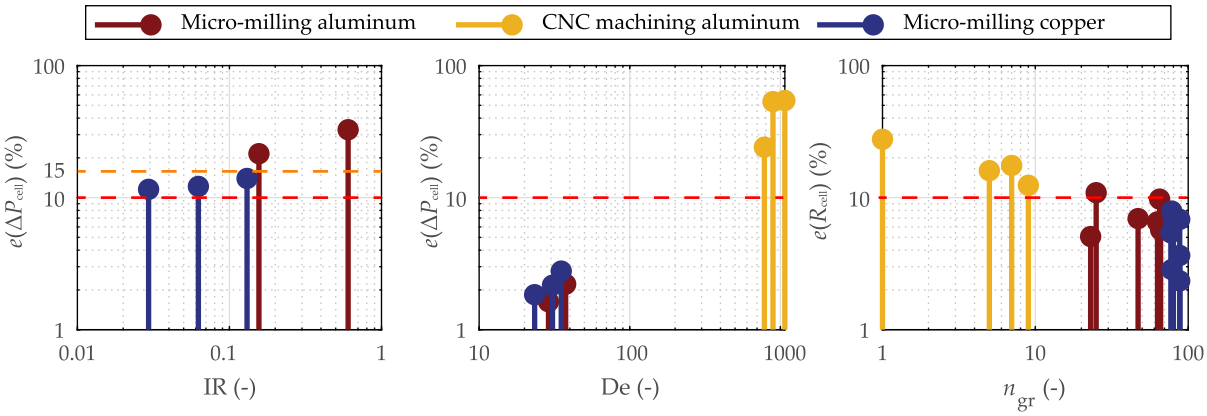

Fig. 6. Relative discrepancy in pressure drop and thermal resistance estimation between the Thermal-Hydrodynamic Model and numerical simulations due to variations in the IR, Dean number, and number of grooves.

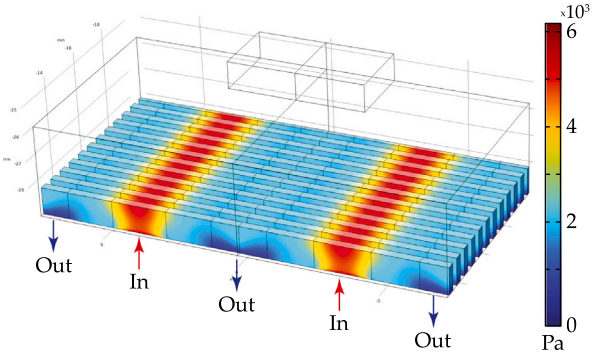

(a) Micro-milling of aluminum: IR = 0.60, VR = 1, and $e\left(\Delta P_{\text{cell}}\right) = 32.7\%$).

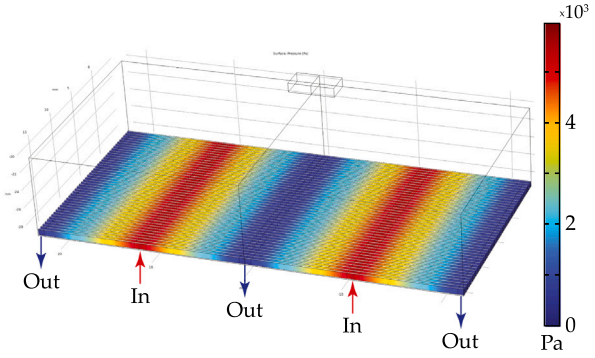

(b) Micro-milling of copper: IR = 0.06, VR = 1, and $e\left(\Delta P_{\text{cell}}\right) = 12.2\%$.

Fig. 7. Pressure distribution for two manifold CGR = 4 configurations. Results shown are from the numerical model.

fluid when changing direction around the bend, thereby introducing so-called Dean vortices.

The case with De = 29 shows a more constant pressure gradient along the channels, as shown in Fig. 8. Here, the impact of the bends is less due to the predominant effect of the long and straight regions and the small Reynolds number. Therefore, the impact on the pressure drop estimation is more pronounced for cases with large Dean numbers due to secondary flow patterns that are becoming more influential.

As shown in Fig. 6, for the serpentine configurations with high Dean numbers between 783 and 893, the THM shows an underestimation of pressure drop of 24.1% and 53.4% respectively. In contrast, for the cases with a Dean number ranging between 23 and 41, lower error estimations of pressure drop up to 2.8% are observed. Hence, for serpentine configurations with a Dean number below 40, the pressure drop estimate error is observed to stay within a 10% margin.

3.3. Impact of number of grooves on heat spreading

Noteworthy is the overestimation of 27.7% in thermal resistance observed for the straight configuration with $n_{\text{gr}} = 1$ (CNC machining). While, the overestimation is less pronounced for the case with $n_{\text{gr}} = 47$ (micro-milling of aluminum), with 6.9%, as highlighted in Table 3.

The number of grooves impacts the assumption regarding the heat-spreading capability. Since a uniform overall HTC at the bottom of the substrate is assumed, this assumption aligns more closely with cases with a high number of grooves. Conversely, in the case of a single groove, heat travels a much shorter distance than the THM assumes. Hence, a relatively low number of grooves leads to overestimating the thermal spreading resistance.

This claim is supported by Fig. 9, illustrating the heat flux distributions for both cases. For the case with $n_{\text{gr}} = 1$, the heat distribution lines curve towards the center line where the single groove is positioned, thereby diminishing the heat traveling distance. In contrast, in the case with $n_{\text{gr}} = 47$, the heat flux is more evenly spread across the channels and the heat transfer path is better estimated.

In this study, the smallest number of grooves found to maintain the relative discrepancy in thermal resistance estimate below 10% is 23. In this case, the thermal resistance is overestimated by 5.1%.

4. Application example

To demonstrate the applicability of the THM for the design of cold plates with multiple heat sources, a case study is presented. This case study integrates the THM with a brute-force search algorithm that systematically explores combinations of distribution schemes and microchannel configurations. By evaluating these combinations, the algorithm identifies the configuration that minimizes cooling power consumption while adhering to a predefined set of design constraints. While the brute-force search is effective, other strategies such as integrated design methods [41] with broader optimization variables and advanced algorithms can also be applied, showcasing the THM's adaptability and robustness for complex thermal management challenges.

4.1. Case definition

In this case study, the initial design of a cold plate designed to accommodate 100 electronic packages, each measuring 5 mm in width and length and dissipating 20 W of heat, is reviewed. The substrate

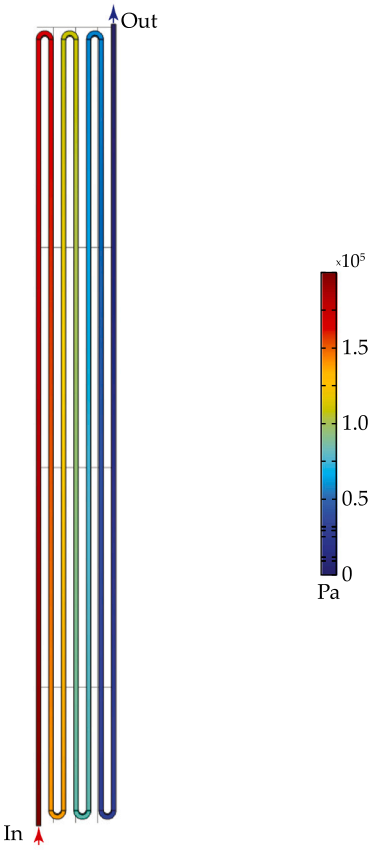

(a) Micro-milling of aluminum: De = 29, and $e\left(\Delta P_{\text{cell}}\right) = 1.6\%$.

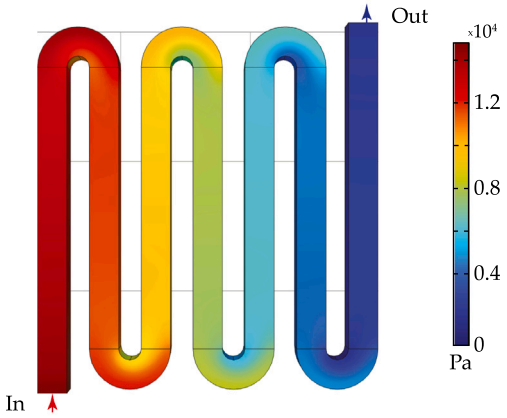

(b) CNC machining aluminum: De = 1071, and $e\left(\Delta P_{\text{cell}}\right) = 54.4\%$.

Fig. 8. Pressure distribution for two serpentine CGR = 1/7 configurations. Results shown are from the numerical model.

thickness is fixed to 5 mm and assumed to be of aluminum with a thermal conductivity of 170 W/m K. Coolant is flown through the channels with an inlet temperature of 20 °C. The TIM is assumed to possess an overall HTC of $k_{\text{TIM}} = 50$ kW/m^2 K, derived from a specific indium-based TIM.

4.2. Constraints

To ensure the practicality and reliability of operation, four key parameters were constrained. The pressure drop was limited to ensure proper coolant distribution by the pump. The coolant flow rate module's coolant flow rate is predefined. Excessively high flow rates hinder the efficient use of the coolant's heat capacity and cause significant pressure drops, while excessively low flows result in large temperature gradients across electrical components, negatively affecting operational efficiency. A maximum package temperature was imposed to prevent overheating, ensuring effective thermal management, while temperature uniformity was prioritized to ensure similar high performance and comparable long-term degradation across all electronic packages. Finally, microchannel geometry was constrained to optimize heat transfer and flow distribution, ensuring manufacturability and system practicality. The pressure drop across the entire cold plate module must fall between a minimum of 0.5 and a maximum of 5 bar. The package temperatures must not exceed 55 °C, and the temperature difference across packages cannot exceed 5 K. Furthermore, the coolant flow rate is constricted to 310 l/h. The microchannel sections are characterized by a maximum allowable width and length of 42 mm. Moreover, the minimum allowable channel width and wall width are both 0.2 mm, and the maximum allowable AR is 3 due to micro-milling manufacturing constraints.

4.3. Method

To maximize the channel heat transfer area, the width and length of the microchannel section and the AR are set to their maximum allowable values, while the channel width and wall width are minimized.

Various design solutions are explored by the THM, including distribution schemes ranging from fully serial ($n_{\text{cl}} = 1$) to fully in parallel ($n_{\text{cl}} = n_{\text{p}}$), with symmetrical hybrid schemes in between. Furthermore, manifold (CGR = 2, 4, and 6), straight (CGR = 1), and serpentine (CGR = 1/3, 1/5, and 1/7) configurations are assessed. These configurations are selected on compatibility with the maximum number of grooves of 105, to maximize heat transfer area and reduce pressure drops.

Finally, the optimal configuration is selected based on minimal pressure drop, thereby minimizing the required cooling power of the system.

4.4. Results and discussion

Fig. 10 presents an overview of the three key performance metrics–maximum package temperature, temperature uniformity across packages, and cold plate module pressure drop–as well as the thermal resistances of the last-cooled package.

Fig. 10(a) demonstrates that there is no significant correlation between the CGR and the maximum package temperature. Transitioning from a manifold with a CGR of 6 to a serpentine with CGR of 1/7 results in a maximum temperature reduction of 0.4 °C when cooling in series ($n_{\text{cl}} = 1$). Although nondiscrimination, the slight reduction is attributed to a higher channel mass flow rate for the serpentine CGR = 1/7 configuration, placing the design into the turbulent flow regime (with Re equal to 15,400), thereby increasing the convective HTC.

The choice of the coolant distribution scheme strongly influences the maximum package temperature. The largest change is observed for the serpentine CGR = 1/7 configuration, reducing the maximum package temperature with of 1.7 °C when transitioning from parallel ($n_{\text{cl}} = n_{\text{p}}$) to serial cooling ($n_{\text{cl}} = 1$). This is attributed to a reduction in thermal spreading and convection resistances, as highlighted in blue and yellow respectively in Fig. 10(b). In this figure, the fluid inlet temperature is expressed as an equivalent thermal resistance (shown in green) relative to the cold plate inlet temperature, to show the impact on the maximum package temperature. Although the figure suggests that the most notable changes are observed in capacitance resistance and fluid inlet temperature (shown in purple and green, respectively) as a function of the number of coolant lines, they are interrelated and counterbalance each other. When the capacitance resistance decreases with more serial-oriented cooling, this positive effect is offset by an increase in the fluid inlet temperature of the last-cooled package.

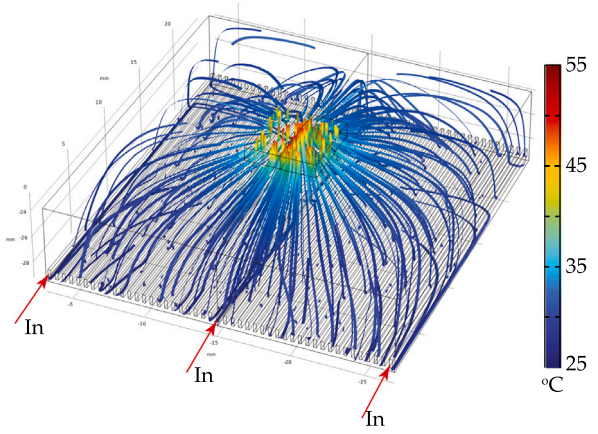

(a) Micro-milling of aluminum: $n_{gr} = 47$, and $e\left(R_{cell}\right) = 6.9\%$.

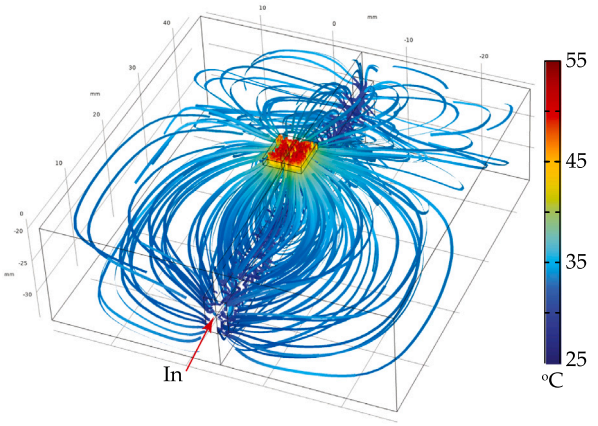

(b) CNC machining aluminum: $n_{gr} = 1$, and $e\left(R_{cell}\right) = 27.7\%$.

Fig. 9. Heat flux distribution of the straight configuration for two cases. Results shown are from the numerical model.

Hence, the coolant distribution scheme primarily influences the thermal spreading and convection resistances. As the number of coolant lines decreases, channel mass flow increases, leading to enhanced convective HTCs, thereby reducing thermal spreading and convection resistances.

Fig. 10(c) illustrates that maximizing the number of coolant lines ($n_{cl} \rightarrow n_p$) results in zero temperature differences across packages. This is because there are no disparities in coolant inlet temperatures across the packages when cooling is 100% parallel. The parabolic behavior of the temperature difference across packages as a function of the number of coolant lines results from the absolute change in local mass flow. This change is the largest when shifting from fully in parallel to the adjacent more serial-oriented hybrid scheme, thereby most significantly increasing the fluid inlet temperature of the last-cooled package. Also illustrated by the figure is the fact that the microchannel configuration does not affect the coolant inlet temperature, hence no correlation between CGR and the maximum difference in package temperature is evident.

Finally, Fig. 10(d) indicates that decreasing both the CGR and the number of coolant lines increases the total pressure drop across the module. The channel mass flow increases when CGR is decreased because fewer channels are present, concentrating the coolant flow to the remaining channels. Similarly, reducing the number of coolant lines results in more serial cooling and increases the channel mass flow. Thus, both parameters are critical for controlling the pressure drop.

4.5. Selection of the optimal configuration

Analysis of the total design space has led to the development of an optimization strategy that focuses on identifying configurations that meet requirements for temperature uniformity, pressure drop, and maximum package temperature.

This strategy, illustrated in Fig. 11, eliminates the necessity to evaluate the entire design space. The initial design starts with the manifold configuration having the highest CGR in conjunction with a fully parallel distribution scheme. This configuration should satisfy the temperature uniformity criterion; otherwise, no solution within the design space is present. If the total pressure drop falls outside the specified limits, the CGR is iteratively reduced until the pressure drop requirement is met. If the maximum package temperature requirement is also satisfied, this configuration is compared with the current optimum configuration. The optimum is selected based on yielding the minimum pressure drop. Following this comparison, the CGR is not further reduced; however, the CGR is reset to its minimum, and the number of coolant lines is reduced to the next feasible distribution scheme. This step prevents the evaluation of lower CGRs for the given number of coolant lines that invariably result in higher pressure drops than previous configurations for the same number of coolant lines. This method continues until a configuration is found that does not meet the temperature uniformity requirement, indicating either that further exploration of the design space is unnecessary or that the entire design space has been thoroughly explored.

Using this procedure, the serpentine CGR = $^1/_5$ configuration with $n_{cl} = 50$ with a module pressure drop of 0.5 bar is identified as optimal. To find this optimum only 30 out of the total 63 configurations had to be evaluated.

Analysis of Fig. 10(a) reveals that all configurations maintain a maximum package temperature below 55 °C (red surface) due to maximized heat transfer area. The orange dots indicate configurations

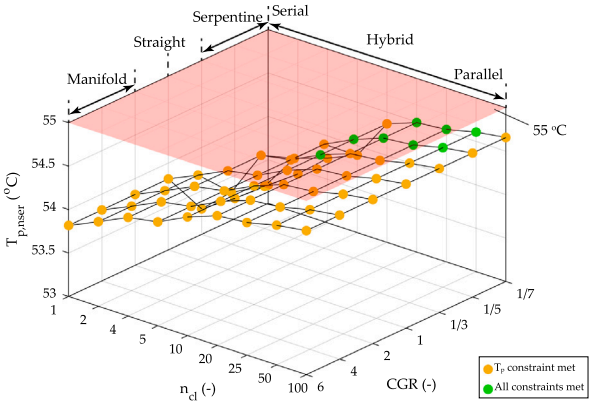

(a) Maximum package temperature.

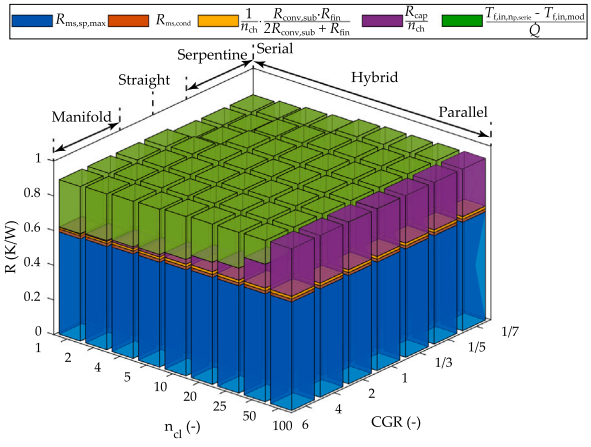

(b) Cold plate unit cell thermal resistance components and fluid inlet temperature of the last-cooled package.

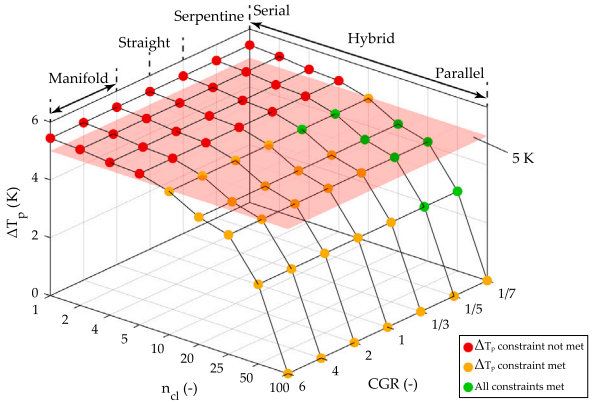

(c) Temperature uniformity across packages.

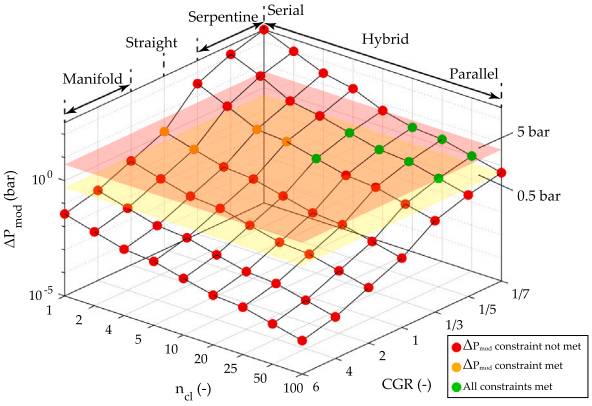

(d) Cold plate module pressure drop.

Fig. 10. Performance characteristics of assessed configurations, spanning from serial to parallel distribution schemes, alongside microchannel configurations encompassing manifold (CGR = 2, 4, and 6), straight (CGR = 1), and serpentine (CGR = 1/3, 1/5, and 1/7). Results are established using the Thermal-Hydrodynamic Model.

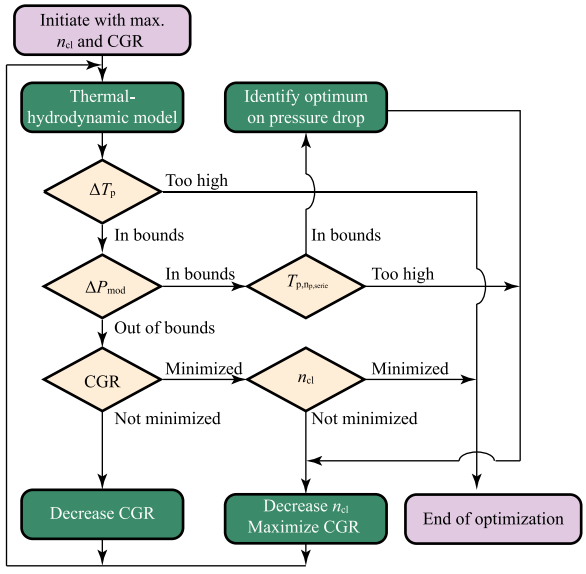

Fig. 11. Cooling scheme optimization strategy.

that meet this specific requirement. The green dots indicate configurations meeting all three requirements: maximum package temperature, temperature uniformity, and module pressure drop. In the charts depicting temperature uniformity and module pressure drop, the red dots represent configurations that did not meet the specific requirement. As shown in Fig. 10(c), only configurations with a more parallel-oriented cooling scheme $(10 \leq n_{cl} \leq 100)$ meet the requirement of keeping the temperature difference across packages below 5 K (red surface). Fig. 10(d) shows the module pressure drop for all combinations, with the yellow surface depicting the minimum pressure drop requirement and the red surface the maximum. It appears that seven other serpentine configurations would have met all constraints, with respective pressure drops ranging from 1.0 to 2.6 bar.

5. Conclusion

This study presents a novel analytical tool that provides a rapid and practical alternative to conventional simulation-based methods for evaluating the thermal performance of manifold, straight, and serpentine microchannel configurations in multi-heat source cold plate designs. By streamlining the initial design process, the Thermal Hydrodynamic Model facilitates the rapid identification of optimal cooling solutions that satisfy system requirements. The model represents a significant advancement in thermal management system design for high-tech industries and serves as a valuable asset for both researchers and engineers.

The findings underscore the considerable potential of the model for assessing the package temperature, temperature uniformity across

packages, thermal resistances, and pressure drop of the microchannel cold plate module. The study has assessed the validity of the results, with the goal of maintaining an error margin of no more than 10% compared to numerical simulations. Pressure drop estimates for straight channels consistently fall within this margin, while for serpentine microchannels this accuracy is achieved when the configurations have a Dean number of no more than 40. For manifold configurations, the error margin of 10% for the pressure drop estimate is not guaranteed, and the margin was increased to 15%. This threshold is met when the Inlet Ratio is up to 0.13 and the Velocity Ratio is maintained at unity for low Reynolds numbers. Additionally, for thermal resistance estimations, the study finds that designs require no less than 23 grooves to ensure the 10% error margin.

The utility of the model is demonstrated through a practical example showcasing the ability to rapidly gain insights into microchannel designs. The results demonstrate that the coolant distribution scheme has a significant impact on the maximum package temperature, with serial cooling reducing the temperature by lowering thermal spreading and convection resistances. No strong correlation is found between the Channel-Groove Ratio and the maximum package temperature, though a slight reduction is observed when transitioning to a more turbulent flow regime when the Channel-Groove ratio is reduced. Moreover, maximizing the number of coolant lines eliminates temperature differences across packages due to the packages receiving the coolant at the same inlet temperature. Additionally, both a lower Channel-Groove Ratio and fewer coolant lines increase the total pressure drop by concentrating the coolant flow, highlighting the need for careful selection of these parameters to balance thermal performance and pressure drop. The ability to gain these insights almost instantaneously accelerates the initial concept design process, enabling quick, insightful evaluations compared to time-consuming simulation-based approaches.

By combining the model with the proposed optimization strategy, it is possible to identify the optimal coolant distribution scheme and microchannel configuration that results in a cooling power reduction of 2.0 to 5.2 times compared to other configurations within the design space. Remarkably, this optimization required calculating performance for less than 50% of all configurations, further highlighting the efficiency of the Thermal Hydrodynamic Model in expediting the initial concept design phase.

5.1. Future work

The criteria of the Dean number and Inlet ratio not exceeding 40 and 0.13 respectively, with the number of grooves being at least 23 and the Velocity Ratio being unity, offer valuable insights into the accuracy of the Thermal Hydrodynamic Model. It is anticipated that incorporating a larger number of cases could extend the range of validity to higher Dean numbers and Inlet Ratios, as well as lower numbers of grooves. Hence, future endeavors concerning the model will focus on determining the thresholds at which the thermal and hydrodynamic performance exceeds the 10% error estimate.

CRediT authorship contribution statement

D.J.G. Kuiphuis: Writing – original draft. **M.J. Terpstra:** Supervision, Writing – review and editing. **W.W. Wits:** Writing – review and editing. **W. Rohlfs:** Supervision, Writing – review and editing.

Declaration of competing interest

The authors declare that they have no known competing financial interests or personal relationships that could have appeared to influence the work reported in this paper.

Data availability

https://data.mendeley.com/datasets/gwnt75p22n/1.

References

[1] D. Jafari, W.W. Wits, The utilization of selective laser melting technology on heat transfer devices for thermal energy conversion applications: A review, Renew. Sustain. Energy Rev. 91 (2018) 420–442.
[2] Z. Zhang, X. Wang, Y. Yan, A review of the state-of-the-art in electronic cooling, e-Prime - Adv. Electr. Eng. Electron. Energy 1 (2021) 100009.
[3] S. Sohel Murshed, C. Nieto de Castro, A critical review of traditional and emerging techniques and fluids for electronics cooling, Renew. Sustain. Energy Rev. 78 (2017) 821–833.
[4] M.M.R. Kiran K. Ambatipudi, Analysis of conjugate heat transfer in microchannel heat sinks, Numer. Heat Transfer A 37 (7) (2000) 711–731.
[5] R. Beach, W. Benett, B. Freitas, D. Mundinger, B. Comaskey, R. Solarz, M. Emanuel, Modular microchannel cooled heatsinks for high average power laser diode arrays, IEEE J. Quantum Electron. 28 (4) (1992) 966–976.
[6] M.G. Khan, A. Fartaj, A review on microchannel heat exchangers and potential applications, Int. J. Energy Res. 35 (7) (2011) 553–582.
[7] A. Mohammed Adham, N. Mohd-Ghazali, R. Ahmad, Thermal and hydrodynamic analysis of microchannel heat sinks: A review, Renew. Sustain. Energy Rev. 21 (2013) 614–622.
[8] A. Abidi, A. Ahmadi, M. Enayati, S.M. Sajadi, H. Yarmand, A. Ahmed, G. Cheraghian, A review of the methods of modeling multi-phase flows within different microchannels shapes and their applications, Micromachines 12 (9) (2021) 1113.
[9] D. Tuckerman, R. Pease, High-performance heat sinking for VLSI, IEEE Electron Device Lett. 2 (5) (1981) 126–129.
[10] X. Peng, G. Peterson, Convective heat transfer and flow friction for water flow in microchannel structures, Int. J. Heat Mass Transfer 39 (12) (1996) 2599–2608.
[11] H. Wu, P. Cheng, An experimental study of convective heat transfer in silicon microchannels with different surface conditions, Int. J. Heat Mass Transfer 46 (14) (2003) 2547–2556.
[12] H. Wang, J.W. Rose, Film Condensation in Horizontal Microchannels: Effect of Channel Shape, in: International Conference on Nanochannels, Microchannels, and Minichannels, 2005, pp. 729–735.
[13] A. Sakanova, C.C. Keian, J. Zhao, Performance improvements of microchannel heat sink using wavy channel and nanofluids, Int. J. Heat Mass Transfer 89 (2015) 59–74.
[14] G. Xia, J. Jiang, J. Wang, Y. Zhai, D. Ma, Effects of different geometric structures on fluid flow and heat transfer performance in microchannel heat sinks, Int. J. Heat Mass Transfer 80 (2015) 439–447.
[15] R. Vinoth, B. Sachuthananthan, A. Vadivel, S. Balakrishnan, A.G.S. Raj, Heat transfer enhancement in oblique finned curved microchannel using hybrid nanofluid, Int. J. Therm. Sci. 183 (2023) 107848.
[16] H. Shafeie, O. Abouali, K. Jafarpur, G. Ahmadi, Numerical study of heat transfer performance of single-phase heat sinks with micro pin-fin structures, Appl. Therm. Eng. 58 (1) (2013) 68–76.
[17] A. Gönül, A. Okbaz, N. Kayaci, A. Selim Dalkilic, Flow optimization in a microchannel with vortex generators using genetic algorithm, Appl. Therm. Eng. 201 (2022) 117738.
[18] A.F. Al-Neama, N. Kapur, J. Summers, H.M. Thompson, An experimental and numerical investigation of the use of liquid flow in serpentine microchannels for microelectronics cooling, Appl. Therm. Eng. 116 (2017) 709–723.
[19] K. Yang, C. Zuo, A novel multi-layer manifold microchannel cooling system for concentrating photovoltaic cells, Energy Convers. Manage. 89 (2015) 214–221.
[20] H. Shen, H. Liu, X. Shao, G. Xie, C.-C. Wang, Thermofluids performances on innovative design with multi-circuit nested loop applicable for double-layer microchannel heat sinks, Appl. Therm. Eng. 219 (2023) 119699.
[21] H. Shen, Z. Zhang, X. Ge, H. Liu, G. Xie, C.-C. Wang, Thermal analysis and experimental verification on double-layer microchannel heat sinks with impact jet nested arrays, Int. J. Heat Mass Transfer 209 (2023) 124169.
[22] X. Cao, X. Lan, S. Gao, C.-C. Wang, H. Shen, Thermal-dynamic analysis research on the designed impingement-jet double-layer nested microchannel heat sinks with vertical truncated bifurcation, Appl. Therm. Eng. 243 (2024) 122585.
[23] G. Lu, Y. Ye, J. Wang, B. Jiao, Y. Kong, R. Liu, Embedded manifold microchannel cooling for chiplet thermal management, in: 2024 23rd IEEE Intersociety Conference on Thermal and Thermomechanical Phenomena in Electronic Systems, ITherm, 2024, pp. 1–5.
[24] G. Bognár, G. Takács, P.G. Szabó, A novel approach for cooling chiplets in heterogeneously integrated 2.5-d packages applying microchannel heatsink embedded in the interposer, IEEE Trans. Compon. Packag. Manuf. Technol. 13 (8) (2023) 1155–1163.
[25] R. van Erp, G. Kampitsis, E. Matioli, Efficient microchannel cooling of multiple power devices with compact flow distribution for high power-density converters, IEEE Trans. Power Electron. 35 (7) (2020) 7235–7245.

[26] X. Wei, Y. Joshi, M.K. Patterson, Experimental and numerical study of a stacked microchannel heat sink for liquid cooling of microelectronic devices, J. Heat Transfer 129 (10) (2007) 1432–1444.
[27] M.K. Moharana, G. Agarwal, S. Khandekar, Axial conduction in single-phase simultaneously developing flow in a rectangular mini-channel array, Int. J. Therm. Sci. 50 (6) (2011) 1001–1012.
[28] G. Wang, L. Hao, P. Cheng, An experimental and numerical study of forced convection in a microchannel with negligible axial heat conduction, Int. J. Heat Mass Transfer 52 (3) (2009) 1070–1074.
[29] Y.-T. Yang, F.-H. Lai, Numerical study of flow and heat transfer characteristics of alumina-water nanofluids in a microchannel using the lattice Boltzmann method, Int. Commun. Heat Mass Transfer 38 (5) (2011) 607–614.
[30] Y.-T. Yang, F.-H. Lai, Lattice Boltzmann simulation of heat transfer and fluid flow in a microchannel with nanofluids, Heat Mass Transfer 47 (10) (2011) 1229–1240.
[31] K.C. Cheng, F.P. Yuen, Flow visualization studies on secondary flow patterns in straight tubes downstream of a 180 deg bend and in isothermally heated horizontal tubes, J. Heat Transfer 109 (1) (1987) 49–54.
[32] S. Lee, Constriction/spreading resistance model for electronics packaging, in: Proceedings of ASME/JSME Thermal Engineering Conference, Vol. 4, 1995.
[33] R.J. Phillips, Microchannel heat sinks, Adv. Therm. Model. Electron. Compon. 2 (3) (1990) 109–184.
[34] P.-S. Lee, S.V. Garimella, Thermally developing flow and heat transfer in rectangular microchannels of different aspect ratios, Int. J. Heat Mass Transfer 49 (17) (2006) 3060–3067.
[35] R.K. Shah, A.L. London, Laminar flow forced convection in ducts: A source book for compact heat exchanger analytical data, in: Advances in Geophysics, Academic Press, 1978.
[36] V. Gnielinski, New equations for heat and mass transfer in turbulent pipe and channel flow, Int. Chem. Eng. 16 (2) (1976) 359–367.
[37] S. Kandlikar, S. Garimella, D. Li, S. Colin, M.R. King, Heat Transfer and Fluid Flow in Minichannels and Microchannels, Elsevier, 2005.
[38] R.J. Phillips, Forced-convection, liquid-cooled, microchannel heat sinks (Master's thesis), Massachusetts Institute of Technology, 1987.
[39] O.C. Jones Jr., An improvement in the calculation of turbulent friction in rectangular ducts, J. Fluids Eng. 98 (2) (1976) 173–180.
[40] H. Zhang, D. Pinjala, T. Wong, K. Toh, Y. Joshi, Single-phase liquid cooled microchannel heat sink for electronic packages, Appl. Therm. Eng. 25 (10) (2005) 1472–1487.
[41] W.W. Wits, J. Jauregui-Becker, F.E. van Vliet, G. te Riele, Developing an integrated design strategy for chip layout optimization, in: Proc. 21st CIRP Des. Conf. Korea 2011 Interdiscip. Des, 2011, pp. 55–62.